

Colossal X-Ray-Induced Persistent Photoconductivity in Current-Perpendicular-to-Plane Ferroelectric/Semiconductor Junctions

Wei Jin Hu, Tula R. Paudel, Sergei Lopatin, Zhihong Wang, He Ma, Kewei Wu, Ashok Bera, Guoliang Yuan, Alexei Gruverman, Evgeny Y. Tsymbal,* and Tom Wu*

Persistent photoconductivity (PPC) is an intriguing physical phenomenon, where electric conduction is retained after the termination of electromagnetic radiation, which makes it appealing for applications in a wide range of optoelectronic devices. So far, PPC has been observed in bulk materials and thin-film structures, where the current flows in the plane, limiting the magnitude of the effect. Here using epitaxial Nb:SrTiO₃/Sm_{0.1}Bi_{0.9}FeO₃/Pt junctions with a current-perpendicular-to-plane geometry, a colossal X-ray-induced PPC (XPPC) is achieved with a magnitude of six orders. This PPC persists for days with negligible decay. Furthermore, the pristine insulating state could be fully recovered by thermal annealing for a few minutes. Based on the electric transport and microstructure analysis, this colossal XPPC effect is attributed to the X-ray-induced formation and ionization of oxygen vacancies, which drives nonvolatile modification of atomic configurations and results in the reduction of interfacial Schottky barriers. This mechanism differs from the conventional mechanism of photon-enhanced carrier density/mobility in the current-in-plane structures. With their persistent nature, such ferroelectric/semiconductor heterojunctions open a new route toward X-ray sensing and imaging applications.

areas such as bistable optical switches,^[4,5] holographic memories,^[6] and bioelectronics.^[7] While most of the works on PPC were carried out with visible and UV light,^[6–11] X-ray-induced PPC (XPPC) has also been observed in a number of different materials including manganites,^[2,3] AlGaAs semiconductors,^[12] and VO₂ films.^[13] Regardless of the illumination sources, basic features of PPC include the slow relaxation of the conductivity after the termination of photon excitation and the efficient recovery of the pristine insulating state through thermal annealing.^[9,13–15] In terms of materials and device configurations, the investigations on PPC in recent decades have mainly focused on semiconductor bulks^[2,6,8] or films^[9–13] (Figure 1a) and their planar heterostructures, where the current flows in the plane of the film^[14,16–18] (Figure 1b). The key mechanism of PPC in these systems is that the microscopic energy barriers suppress the

recombination of electrons and holes once they are photoexcited. The origin of these energy barriers, however, depends strongly on the characteristics of the materials and their configurations. For example, in bulk semiconductors or thick films, the microscopic barriers at the atomic level originate

1. Introduction

Persistent photoconductivity (PPC), i.e., electromagnetic radiation induced conduction that can persist for a long time after the termination of illumination,^[1–3] has potential applications in

Dr. W. J. Hu, Dr. K. W. Wu, Dr. A. Bera, Prof. T. Wu
Materials Science and Engineering
King Abdullah University of Science and Technology
Thuwal 23955-6900, Saudi Arabia
E-mail: Tao.Wu@kaust.edu.sa

Dr. W. J. Hu
Shenyang National Laboratory for Materials Science
Institute of Metal Research (IMR)
Chinese Academy of Sciences (CAS)
Shenyang 110016, China

Prof. T. R. Paudel, Prof. A. Gruverman, Prof. E. Y. Tsymbal
Department of Physics and Astronomy, and Nebraska Center
for Materials and Nanoscience
University of Nebraska
Lincoln, NE 68588, USA
E-mail: tsymbal@unl.edu

Dr. S. Lopatin
Imaging and Characterization Core Lab
King Abdullah University of Science and Technology (KAUST)
Thuwal 23955-6900, Saudi Arabia

Dr. Z. H. Wang
Advanced Nanofabrication Core Lab
King Abdullah University of Science and Technology (KAUST)
Thuwal 23955-6900, Saudi Arabia

Dr. H. Ma, Prof. G. L. Yuan
School of Materials Science and Engineering
Nanjing University of Science and Technology
Nanjing 210094, P. R. China

 The ORCID identification number(s) for the author(s) of this article can be found under <https://doi.org/10.1002/adfm.201704337>.

DOI: 10.1002/adfm.201704337

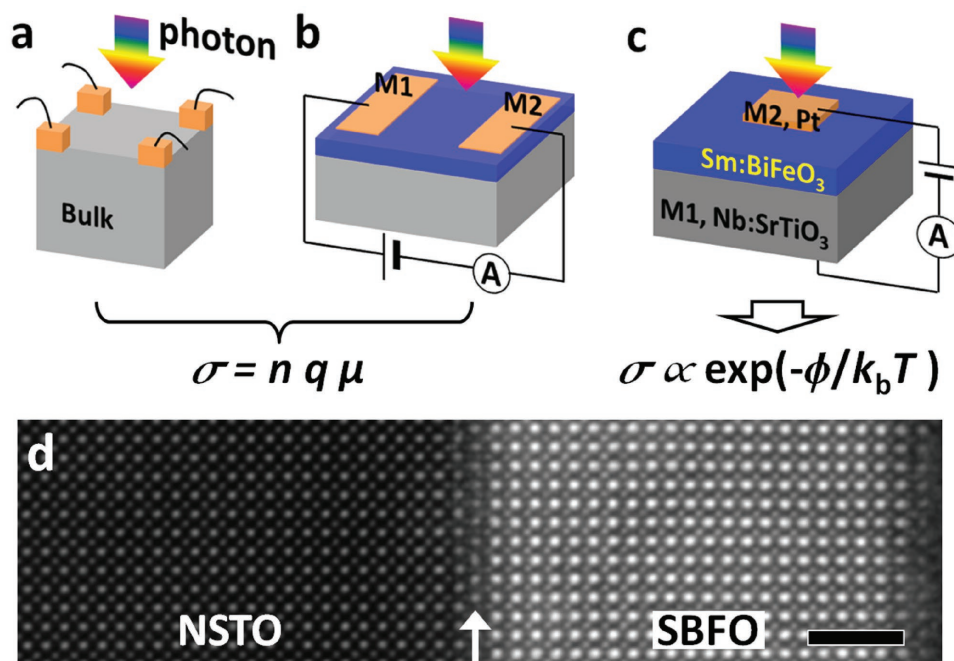


Figure 1. Planar versus perpendicular device architectures for acquiring persistent photoconductivity. a) Bulk crystal. b) Current-in-plane thin film structure. c) Current-perpendicular-to-plane heterostructure with an X-ray-modulated ferroelectric/semiconductor barrier. M1 (2) denote metallic electrodes. Unlike (a) and (b), X-ray-induced modulation of the interfacial energy barrier (ϕ) in (c) contributes directly to the enhancement of conductivity (σ), giving rise to the colossal XPPC observed in this work. d) HR-STEM image of the as-deposited SBFO (9 nm) film grown on the NSTO substrate. The arrow denotes the sharp interface. Scale bar, 2 nm.

from defect-related traps as reported for SrTiO_3 ,^[6] VO_2 ,^[13] and BiFeO_3 ,^[9] or from random composition variations as reported for $\text{Zn}_{0.3}\text{Cd}_{0.7}\text{Se}$.^[8] In semiconductors like GaAs alloys^[10,19] and ZnO films, PPC was proposed to be related to DX centers which are deep-level traps undergoing lattice distortion after photon excitation.^[20] For planar semiconductor heterostructures (Figure 1b), such as n-GaAs/p-GaAs, and $\text{LaAlO}_3/\text{SrTiO}_3$, a macroscopic junction barrier is believed to spatially separate the photoexcited electron/hole pairs in the in-plane transport and thus account for the PPC effect.^[14,16,18]

A common feature of these PPC structures is that the electric transport was measured in plane, and the PPC effect is limited by the modulation of the photon-sensitive layers themselves. The magnitude of the reported PPC effect is moderate because of the limited carrier density/mobility (n/μ) modulation of the active materials.^[6–17] The energy barriers suppress the recombination of photoexcited electron/hole pairs, which, however, do not contribute directly to the in-plane enhanced conductivity. On the other hand, a drastically different scenario of charge transport occurs in thin-film junctions (Figure 1c), where the current flows perpendicular to the plane and thus the conductivity (σ) is extremely sensitive to the interfacial electronic properties, particularly interfacial barrier (ϕ). The latter can be modulated by photon stimulation, which is expected to lead to an exponentially enhanced PPC effect.

In this paper, we propose a thin-film heterostructure (Figure 1c) with an insulating ferroelectric layer ($\text{Sm}_{0.1}\text{Bi}_{0.9}\text{FeO}_3$) being sandwiched between two electrodes (Nb:SrTiO₃ and Pt) as a new device scheme to produce a significantly enhanced XPPC

effect. Similar heterostructures have been used as ferroelectric capacitor^[21] and tunnel junctions,^[22–24] but there has been no report of PPC effect in such perpendicular ferroelectric/semiconductor junctions. In the Nb:SrTiO₃/ $\text{Sm}_{0.1}\text{Bi}_{0.9}\text{FeO}_3$ /Pt heterostructures, we observed a colossal PPC effect triggered by X-ray illumination with an unprecedented conductivity enhancement of six orders of magnitude, which was retained for days at room temperature after the termination of illumination.

2. Results

2.1. X-Ray-Induced Persistent Photoconductivity

Epitaxial $\text{Sm}_{0.1}\text{Bi}_{0.9}\text{FeO}_3$ (SBFO) films were deposited on (001) 0.7 wt% Nb:SrTiO₃ (NSTO) conducting substrates using pulsed laser deposition (PLD). Structural characterization of the NSTO/SBFO heterostructures was performed using the aberration-corrected scanning transmission electron microscopy (STEM) combined with electron energy loss spectroscopy (EELS) (see the Experimental Section for details). High-angle annular dark-field image (Figure 1d) confirmed the high-quality epitaxial growth of the SBFO film on NSTO substrate. NSTO heterostructures with different top metal electrodes (Al, Ti, Au, and Pt) and NSTO/SBFO/Pt sandwiched capacitor devices were prepared by using photolithography (see the Experimental Section for details). Figure 2a shows an atomic force microscopy (AFM) topographic image of the 9 nm SBFO film, which reveals a smooth surface with a root-mean-square-roughness of

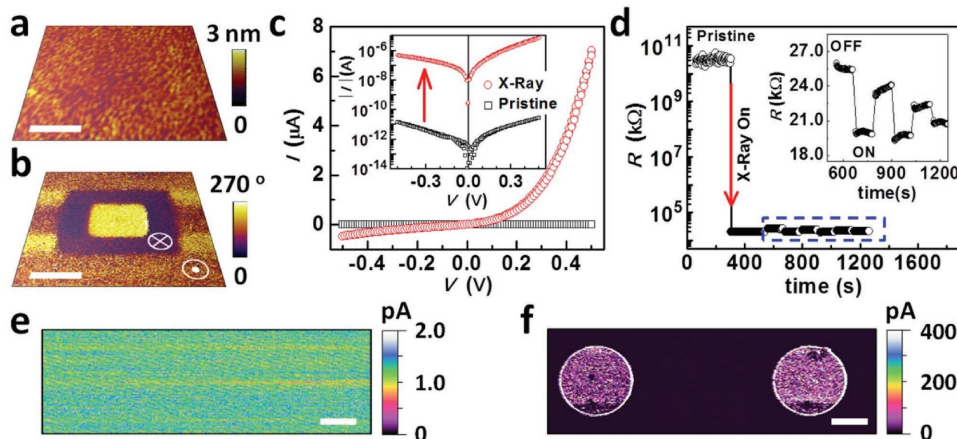


Figure 2. Observation of the XPPC effect in the NSTO/SBFO (9 nm) heterostructure. a) AFM image of the 9 nm SBFO film. b) PFM phase image of square domains with downward and upward polarizations written with +4 V and then -4 V bias on the SBFO film. c) I - V curves measured before and after X-ray illumination on the heterostructure. The inset shows the semilogarithmic plot of the same data. d) Persistent resistance change induced by X-ray illumination measured at a bias of 0.2 V. The inset shows the consecutive switching of the heterojunction resistance in the XPPC state. CAFM images of e) the pristine state for the as-deposited NSTO/SBFO (9 nm) film and f) the XPPC state acquired after X-ray illumination through a mask with circular holes. Scale bars: 1 μm in (a) and (b); 10 μm in (e) and (f).

0.3 nm over an area of $4 \times 4 \mu\text{m}^2$. Figure 2b shows the out-of-plane piezoresponse force microscopy (PFM) phase image of the same film after writing square areas with +4 V and then -4 V dc bias applied on the conducting tip. A 180° phase contrast of opposite domains confirms the ferroelectric nature of the film. Because the as-grown film has the same phase contrast as the domains after -4 V writing, the self-polarization of the as-grown films is pointing up. Such a preferred polarization state is usually attributed to the built-in electric field.^[25]

To check the X-ray response of the heterojunctions, we expose them to the homogeneous illumination of broad-spectrum X-ray with a low dose rate of $140 \mu\text{Gy s}^{-1}$ (see the Experimental Section for details). Figure 2c shows the typical I - V curves of the NSTO/SBFO (9 nm)/Pt heterostructure devices measured before and after X-ray illumination. The pristine state before illumination shows relatively low conductivity with a current on the order of picoampere (pA). After illumination, the current is markedly enhanced by 5–6 orders across the whole range of voltage bias. This tremendous enhancement of conductivity is also confirmed by the time-dependent resistance measurement before and after X-ray illumination, as shown in Figure 2d. An abrupt resistance drop by six orders of magnitude was observed. Importantly, this photoconductivity effect has a persistent nature, i.e., once the device is in the low resistance state after X-ray illumination, the following X-ray switching on and off only produces negligible resistance modulations, as shown in the inset of Figure 2d. In such current-perpendicular-to-plane heterostructures, the PPC magnitude ($\approx I_{\text{ppc}}/I_{\text{pristine}}$) reaches an unprecedented high value of 10^6 . This enhanced conductivity persists for a long time, which will be discussed in more details in a later section.

The persistent resistance change observed here is different from the polarization-induced switching effect achieved in tunnel junctions under the stimulation of an external electric field,^[24] because there is no polarization reversal of the SBFO

layer induced by X-ray illumination, which was confirmed by the identical local PFM phase of the pristine state and the XPPC state (Figure S1, Supporting Information).

The XPPC effect observed here also differs from the photovoltaic (PV) effect observed in such ferroelectric/semiconductor heterostructures (Figure S2, Supporting Information). For the PV effect, a large transient photocurrent with an on/off ratio up to $\approx 10^4$ was achieved under a 365 nm (3.4 eV) light illumination, but the junction current almost returned to the same level after the light was turned off. The PPC magnitude is only ≈ 3 , which is much smaller than the colossal PPC induced by X-ray. This fact suggests that high photon energies above the band gap of semiconducting NSTO are required in producing a considerable PPC effect in our heterostructure. A similar phenomenon was observed in manganite crystal^[2,3,15] and VO_2 film.^[13] Furthermore, we note that this effect differs from the UV light induced resistance decrease observed in SrTiO_3 single crystal,^[6] where sub-band gap photons (2.9 eV) could trigger the PPC effect. Such a difference may originate from the different materials and device configurations we used. The SrTiO_3 single crystal used in the previous report for achieving PPC is a weak p-type semiconductor with a low carrier density of $\approx 5 \times 10^{15} \text{ cm}^{-3}$ and a high resistivity of $\approx 290 \Omega \cdot \text{cm}$, whereas the NSTO substrate used here is an n-type semiconductor showing metallic behavior with a carrier density as high as $\approx 2 \times 10^{20} \text{ cm}^{-3}$ and a low resistivity of $\approx 4.2 \text{ m}\Omega \cdot \text{cm}$ (Figure S3, Supporting Information). More importantly, as we will show below, the XPPC observed here is closely related to the X-ray-induced modification of the SBFO/NSTO interfacial region, rather than a bulk effect.

The XPPC effect was also confirmed by the local electric measurement on the NSTO/SBFO (9 nm) thin film heterostructure using conductive atomic force microscopy (CAFM). A dc bias of 0.5 V was applied on the bottom electrode when the CAFM image was acquired. As shown in Figure 2e, the CAFM mapping of the as-deposited pristine sample shows a

homogeneous low current on the level of pA, suggesting the highly insulating nature of the as-deposited film. However, after X-ray illumination on the sample through a shadow mask with circular holes, the current level in the illuminated regions is increased by almost three orders of magnitude (Figure 2f), which suggests the prospect of local resistance switching in such ferroelectric/semiconductor heterostructure thin films using X-ray probes.

2.2. Relaxation Behavior of XPPC and Thermal Recovery of the Pristine State

To characterize the XPPC effect of the NSTO/SBFO/Pt heterostructure, we monitored the current relaxation behavior for devices with an SBFO thickness of 9 nm. Figure 3a shows the I - V curves of the PPC state recorded at various times up to 1452 h (60.5 d) after X-ray illumination. Due to the decay of the current, the PPC magnitude decreases with time, but remains larger than $\approx 10^4$ after two months. Figure 3b is the typical current relaxation data measured at a 0.2 V bias, showing that the current experiences a sharp decrease during the initial 20 h, followed by a flat tail afterward. We found that this relaxation behavior fitted well with the stretched exponential function^[8,13,16,18,26]

$$I_{\text{PPC}}(t) = I_{\text{PPC}}(0) \exp(-(t/\tau)^\beta) \quad (1)$$

where τ is the relaxation time constant and β is the decay exponent ($0 < \beta < 1$). This function is commonly used to describe disordered systems relaxing toward equilibrium.^[27,28] It is suitable to describe the PPC relaxation in these terms, because the microscopic energy barriers which are responsible for the PPC effect originate from disordered composition fluctuation or discrete traps.^[8,13,29,30] As β approaches one, the function approaches the classical single-exponential behavior, and different microscopic relaxation events become independent and indistinguishable.^[27]

The inset of Figure 3b shows that the plot of $\ln[\ln(I_0/I_t)]$ versus $\ln t$ can be fitted well with two straight lines of different slopes that crossover at ≈ 21 h. In other words, the XPPC decay can be described by two consecutive stretched exponentials with a τ of 0.57 and 0.008 h, and with a β of 0.24 and 0.11, respectively, for the two time regions. The average relaxation time can be calculated through $\langle \tau \rangle = \beta^{-1} \tau \Gamma(\beta^{-1})$ with Γ being the γ function,^[13,29] which are ≈ 17.6 and ≈ 4066 h, representing the initial fast decay and the subsequent slow decay of the XPPC current, respectively. Such a relaxation crossover behavior was theoretically predicted and experimentally observed in polymer chain dynamics,^[31] and now it is observed in an electronic system.

Because PPC relaxation is usually related to discrete traps, and detrapping of the charge carriers is a phonon-assisted thermal excitation process, the excitation time can be described by a simple Arrhenius model^[13]

$$t = t_0 \exp(E_a/k_B T) \quad (2)$$

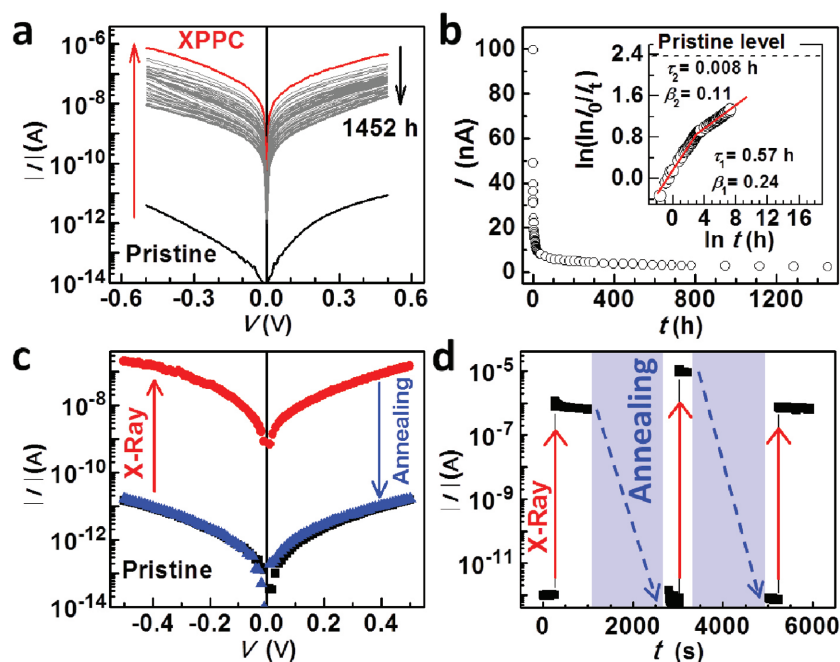


Figure 3. Relaxation of the XPPC state and thermal recovery of the pristine state. a) I - V curves of the XPPC state measured on the NSTO/SBFO (9 nm)/Pt heterostructure as a function of time up to 1452 h (60.5 d). I - V curve of the pristine state is shown for comparison. b) Current versus time at a bias of 0.2 V obtained from (a). Inset is the same data plotted in the form of stretched exponential, and the red lines are the corresponding fittings with a crossover occurring at ≈ 21 h. c) I - V curves of the pristine state (black), the XPPC state (red) and the state after annealing at 473 K for 30 min (blue). d) Reversible conductance modulation during alternative of X-ray illumination and thermal annealing processes.

where t_0 is the carrier lifetime and E_a is the activation energy. By using a carrier lifetime of ≈ 100 ns,^[32] and the two average relaxation times of 17.6 and 4066 h, we can estimate the two average activation energies for the two relaxation-time regions as 0.69 and 0.83 eV. The relaxation crossover with different activation energies may come from the energy redistribution of traps.

Table 1 compares the XPPC parameters measured in our experiments with the previous reports.^[6,9,11,13,14,17] We obtained an unprecedented large XPPC effect with a magnitude up to 10^6 . The average decay times of ≈ 17.6 and ≈ 4066 h are comparable with those observed in VO_2 films^[13] and Si membranes.^[11] This long decay time is several orders of magnitude larger than the lifetime of charge carriers, suggesting the relatively slow relaxation nature of XPPC. Exponent β reflects the distribution of defect traps and relates to the dimensionality of charge transport.^[13,27] For a thermally assisted relaxation process of carrier detrapping, β equals 3/7, 1/3, or 1/5 for 3, 2, or 1D systems with strong electron correlations, respectively.^[13,27] Our observed values of $\beta = 0.24$ and 0.11 are close to that of the 2D AlGaIn/GaN heterostructure (≈ 0.3).^[17] In contrast, they are much

Table 1. Comparison of room-temperature PPC parameters of typical materials and heterostructures.

Material	Magnitude of PPC	Average relaxation time (τ)	Illumination source	Reference
AlGaIn/GaN	≈ 3	2.8 h	Mercury/neon lamp	[17]
VO ₂	≈ 10	69 h	X-ray [10.3 keV]	[13]
BiFeO ₃	282	2.1 h	405 nm at 80 mW	[9]
SrTiO ₃	483	–	410 nm Xe lamp	[6]
Si membranes	10 ³	37	Fluorescent lamp	[11]
STO/LAO	10 ⁵	–	395 nm/visible light	[14]
NSTO/BFO/Pt	10 ⁶	17.6 h 4066 h	Broad spectrum X-ray	This work

smaller than those of 3D systems such as VO₂ films (0.69)^[13] and Si membranes (0.59).^[11]

Regarding potential applications, it is important to operate the heterojunctions repeatedly between the high and low-conductance states. This reliable operation requires finding a protocol to recover the pristine state after the device is switched to the high-conductance XPPC state. Thermal treatment has been used for this purpose,^[6,9,13,14,33] which could provide activation energy for the carriers to escape from the trapping centers. By annealing the device in the XPPC state to different temperatures and monitoring its I – V curve at room temperature after cooling down (Figure S4, Supporting Information), we found that an annealing treatment at 473 K for ≈ 30 min is sufficient to return the current to the pristine state. As shown in Figure 3c, X-ray illumination switched the pristine state to the high-conductance XPPC state, whereas the thermal annealing procedure brought the junction back to the low-conductance pristine state. The recovery of the pristine state was also confirmed by monitoring the junction current at a 0.2 V bias during the thermal process (Figure S5, Supporting Information).

Such an annealing-assisted recovery of the pristine state allowed us to realize consecutive stable switching between the low and high-current states via alternating illumination and annealing procedures (Figure 3d). This reliable and reproducible switching operation, together with the superb XPPC property, make such ferroelectric/semiconductor heterostructures promising for applications as nonvolatile X-ray detectors. The low working voltage (less than 0.5 V) and the miniature device size (5 μm) are promising for integration into pixel-detector arrays for X-ray imaging with high resolution. Furthermore, our CAFM result (Figure 2f) suggests the possibility of direct high-resolution X-ray imaging through resistance mapping after exposure. These operation features cannot be achieved by using the conventional bulk/thin film structures with a current-in-plane configuration. Different with photodetectors based on reversible photoconductive and PV effects, the XPPC detectors can provide a nonvolatile mode of protection during X-ray leak detection, i.e., once it is triggered by external stimulus, it will keep alarming till reset through thermal annealing, similar to the safety protocol widely used in fire-alarm systems.

2.3. Dependence of the XPPC Effect on the Electrode and SBFO Film Thickness

To confirm the dominant role of interfacial barriers in this colossal XPPC effect, we systematically investigated the effect of electrode selection and SBFO thickness on the XPPC characteristics. Typical I – V curves of the pristine state (dark data) and the XPPC state (red data) are shown in Figure 4a–d for heterostructures made of NSTO in direct contact with different top electrodes of Ti, Al, Au, and Pt. The corresponding statistics of PPC magnitude are summarized in Figure 4e. As shown in Figure 4a,b, the high current level and the linear I – V behavior (inset of Figure 4a) suggest that the low work function metals, such as Ti (≈ 4.33 eV) and Al (≈ 4.3 eV), form ohmic contacts with NSTO, and the photoconductive effect is weak because the transport is dominated by the bulk NSTO substrate itself. By contrast, for junctions formed with the high work function metals Au (≈ 5.1 eV) and Pt (≈ 5.6 eV), the current is 4–7 orders smaller (Figure 4c,d), suggesting that the transport is dominated by the interfacial Schottky barrier due to the carrier depletion in NSTO. The large current under the reverse bias indicates a small depletion width as a result of the large carrier concentration in NSTO.^[34] The highly pronounced XPPC in the Schottky junctions (Figure 4e) suggests that the depletion of NSTO in the interface region is a prerequisite for producing the XPPC effect. As the underlying mechanism, X-ray illumination modulates the depletion layer and the interfacial barrier, leading to the XPPC effect.

More importantly, in NSTO/SBFO/Pt heterostructures, the SBFO thickness serves as an additional parameter to tune the XPPC effect. The XPPC effect of NSTO/SBFO/Pt heterostructures with different SBFO thicknesses is shown in Figure 4f–i, and the corresponding XPPC magnitudes are summarized in Figure 4j. The upward ferroelectric polarization of SBFO (Figure 2b) not only enhances the depletion of NSTO and thereby reducing the dark current,^[22–24] but also reduces the recombination of X-ray-induced electron–hole pairs, leading to the colossal magnitude of the XPPC effect. As expected, with SBFO thicknesses of 3 and 9 nm (Figure 4f,g), the conductance differences between the XPPC and the pristine states are significantly enhanced compared to the NSTO/Pt junction. However, upon further increasing the SBFO thickness to 30 and 80 nm (Figure 4h,i), the effect becomes weaker due to the high resistance of the SBFO layer. The maximum XPPC reaches $\approx 10^6$ for the NSTO/SBFO/Pt heterostructure with an SBFO thickness of 9 nm.

When the polarization of SBFO is electrically switched downward to the NSTO electrode, both the NSTO/SBFO/Pt junction conductance and the XPPC effect are greatly reduced (Figure S6, Supporting Information). A downward polarization induces the accumulation of electrons at the NSTO surface to screen the positive polarization charges of SBFO, which suppresses the depletion of NSTO and minimizes the XPPC effect. These observations suggest that the ultrathin SBFO layer with upward polarization is critical for acquiring the optimal XPPC effect, and its barrier formed with the depleted NSTO dictates the junction transport. In fact, both SrTiO₃ crystal^[6] and BiFeO₃ film^[9] have been reported to exhibit PPC, which is also our motivation to choose them as the components to construct our heterojunctions. However, because the transport of the NSTO/SBFO/Pt junction is dominated by the interfacial barriers,

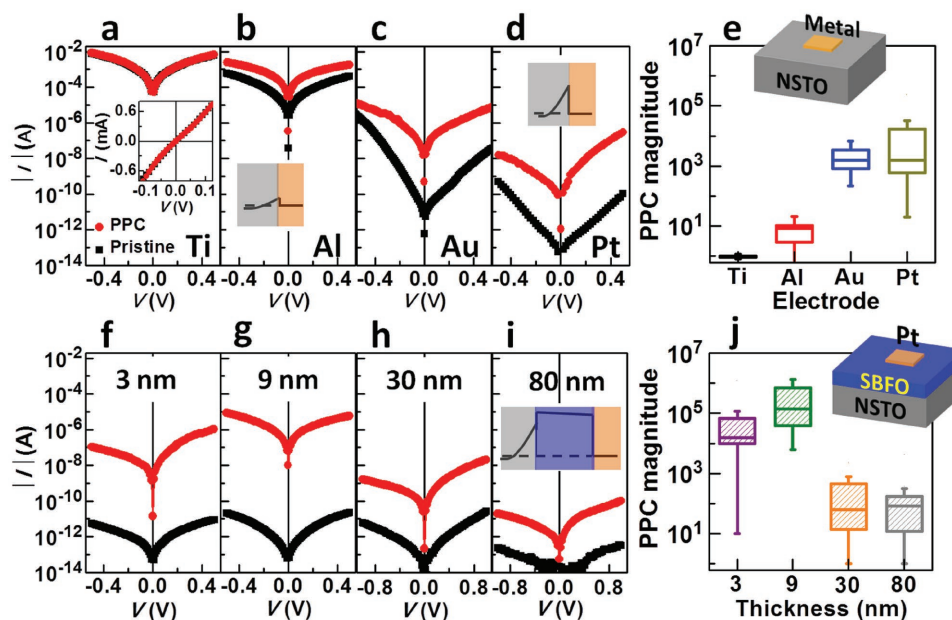


Figure 4. Electrode and SBFO thickness dependence of the XPPC effect. Typical I - V curves of the pristine and XPPC states for the heterostructures of a) NSTO/Ti, b) NSTO/Al, c) NSTO/Au, d) NSTO/Pt. The inset of (a) shows the ohmic transport of the NSTO/Ti junction. f-i) I - V curves of NSTO/SBFO/Pt with SBFO thicknesses of 3, 9, 30, and 80 nm. Insets of (b), (d), and (i) illustrate the schematic band alignments of the heterojunctions. Statistics of XPPC magnitude as a function of electrode and SBFO thickness are shown in (e) and (j), respectively, and 24 devices were measured for each type of samples. Insets of (e) and (j) show the schematic device structures.

the origin of the colossal XPPC effect differs from the planar devices made of individual oxides. The magnitude of the PPC effect in these planar devices is no more than 10^3 , as reported for bulk SrTiO₃ crystal^[6] and BiFeO₃ thin film,^[9] which are three orders smaller than the effect observed here.

2.4. X-Ray Induced Modification of the Interfacial Barrier

To describe the X-ray-induced modification of the energy barriers quantitatively, we further analyzed the conducting mechanisms of the pristine and XPPC states. Several models such as the bulk limited Pool-Frenkel emission,^[35,36] the interface controlled Schottky emission^[37] and the space-charge-limited-current model,^[38] which are commonly used for describing oxide heterojunctions, have been considered (Figure S7, Supporting Information). We found that the I - V data measured on the Pt/SBFO/NSTO heterojunctions could be described well by the Schottky emission model, and the devices can be treated as two diodes connected back-to-back (inset of Figure 5a). Thereby, the junction current is always limited by the diode that is reversely biased,^[39] and accordingly the I - V characteristics can be described by the following equation

$$\ln \frac{J}{T^2} = \ln A^* - \frac{\phi_b}{k_B T} + \frac{q}{k_B T} \sqrt{\frac{qV}{4\pi d \epsilon_0 \epsilon_{op}}} \quad (3)$$

where A^* is the effective Richardson constant, ϕ_b is the Schottky barrier height, d is the SBFO film thickness. k_B is Boltzmann's constant, ϵ_0 is the vacuum permittivity, and ϵ_{op} is the optical dielectric constant of the SBFO film.

As shown in Figure 5a, the simple diode model and the Schottky emission mechanism can satisfactorily explain the observed transport behavior. Importantly, ϕ_b can be estimated from the thermal activation behavior of the temperature dependent I - V curves (Figure S8, Supporting Information). For the pristine state, ϕ_b was estimated to be 0.71 and 0.62 eV for the Pt/SBFO and the NSTO/SBFO interfaces, respectively. These values are close to the theoretical estimation of ≈ 0.9 eV for the barrier formed when BiFeO₃ contacts to Pt or some

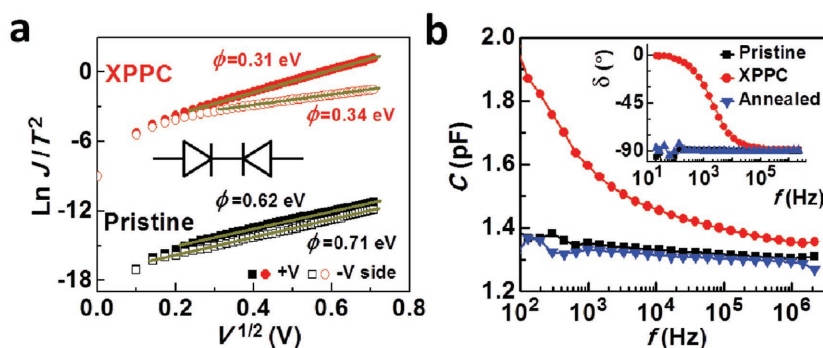


Figure 5. Conducting mechanism and capacitance switching of NSTO/SBFO (9 nm)/Pt heterostructure. a) Schottky emission fittings of the pristine and XPPC states. The inset schematically depicts the back-to-back Schottky diode model. b) The frequency dependent capacitance for the pristine, XPPC, and annealed states. Inset, the corresponding frequency dependent phase angle.

metallic oxides.^[40] By contrast, for the conductive PPC state after illumination, ϕ_b was estimated to be 0.34 and 0.31 eV for the Pt/SBFO and NSTO/SBFO interfaces, respectively. Such a significant reduction of ϕ_b by 0.3–0.4 eV is responsible for the huge enhancement of conductivity from the pristine state to the PPC state. This mechanism intrinsically differs from that proposed previously for current-in-plane heterostructures,^[6–18] in which the enhancement of carrier density or mobility was the dominant factor.

Concurrent with the resistance modulation, we also observed a persistent change of capacitance induced by X-ray illumination, which further helps unravel the origin of the XPPC effect. Figure 5b shows the frequency dependent capacitance data for the pristine, XPPC, and annealed states of a typical device. Clearly, the capacitance of the pristine state is much smaller than that of the PPC state, indicating a reduction of the dielectric layer thickness, which is in line with the thinning of the NSTO depletion layer after X-ray illumination. In addition, in contrast to the capacitance of the pristine state which increases slowly in the low-frequency range, the capacitance of the XPPC state increases sharply below ≈ 2 kHz. Such a significant capacitance enhancement in the low frequency region is usually ascribed to charge trapping at interfaces, and the field distortion caused by the accumulation of these trapped charges increases the overall capacitance of the device at low frequencies.^[41] Quantitatively, we could estimate the depletion region width in NSTO by considering the capacitance of the NSTO/SBFO/Pt heterostructure as the sum of contributions from the NSTO and SBFO capacitance; thereby, the overall capacitance is described by the following equation

$$1/C = 1/C_d + 1/C_F = W_D/\epsilon_o \epsilon_d A + d/\epsilon_o \epsilon_F A, \quad (4)$$

where C_d and C_F are the capacitances of the NSTO depletion layer and the SBFO layer, respectively; W_D and d (9 nm) are the depletion layer width of NSTO and the thickness of SBFO, respectively; ϵ_d and ϵ_F are the dielectric constant of NSTO and SBFO, respectively; A is the junction area, and ϵ_o is the vacuum permittivity. Using $\epsilon_d = 72$ and $\epsilon_F = 122$ at 100 Hz, determined from the capacitance measurement of a SBFO (200 nm) film and a NSTO/Pt Schottky junction (see Figure S9, Supporting Information), respectively, we obtained $W_D = 6.4$ and 2.9 nm for the pristine state and the PPC state, respectively.

The inset of Figure 5b shows the frequency dependent phase angle, δ , of the complex impedance for the pristine, XPPC, and annealed states. A δ of $\approx 90^\circ$ for the pristine state suggests it is close to an ideal capacitor,^[42] due to the depletion of NSTO interface and the high interface barriers. By contrast, it is close to 0° for the XPPC state in the low-frequency region, suggesting that the XPPC state behaves more like a leaky dielectric, due to the X-ray-induced reduction of the NSTO depletion and the interface barriers.

2.5. Microscopic Investigation of the XPPC Effect

It is well known that defects such as oxygen vacancy could play a big role in determining the conductivity of oxide thin films and heterostructures. The type and density of defects can

be controlled during film growth,^[43] and their migration and redistribution could be triggered using external stimuli such as electric field^[3,24,44] and even solvent immersion.^[45] Similarly, PPC effect in the in-plane structures was generally ascribed to the trapping of photon-excited carriers by defects such as DX centers^[20] and oxygen vacancies.^[14] In addition, X-ray irradiation could create defects especially the oxygen vacancies, and to alter the charge and orbital states in strongly correlated metal oxides.^[15,46] These previous reports, together with the observations of slow PPC relaxation and efficient thermal recovery behavior, made us believe that defect generation and electron trapping could be at play in the present perpendicular heterostructures.

To identify the charge-trapping defects and to elucidate the microscopic origin of the XPPC effect, we carried out STEM measurements on a heterostructure (NSTO/SBFO 9 nm) before and after X-ray illumination. Figure 6 shows the high-angle annular dark field (HAADF) and low-angle annular dark field (LAADF) images of a NSTO region near the NSTO/SBFO interface for the pristine sample (Figure 6a,b) and the XPPC sample after X-ray exposure (Figure 6c,d). We note that the low pass filter is applied to both HAADF and LAADF images to enhance the contrast. The raw images are given in Figure S10 in the Supporting Information. The contrast of HAADF images is mainly proportional to $Z^{1.7}$ (Z , atomic number),^[47,48] while LAADF images (additionally to Z contrast) are sensitive to the local strain fields resulted from point defects such as oxygen vacancies.^[49] If oxygen vacancies are present, we expect cloud-like bright spots in the LAADF image, which on the other hand should be absent in the HAADF image in the same specimen area. Indeed, compared to the pristine sample (Figure 6b), a significantly higher concentration of contrast spots was observed in the LAADF image of the XPPC sample (Figure 6d), indicating that the X-ray exposure induced a higher concentration of oxygen vacancies in NSTO.

To quantify the oxygen deficiency, EELS of Ti-L edge (Figure 6e) and O-K edge (Figure S11, Supporting Information) were collected from the NSTO areas near the NSTO/SBFO interface. The variation of EELS edge generally reflects the electronic structure changes pertinent to defects, bonding state, and crystal symmetry, which has been broadly reported in diverse oxides.^[43,49,50] Compared with O-K edge, Ti-L edge is six times more sensitive to oxygen deficiency for NSTO because each ionized oxygen vacancy transforms two Ti^{4+} ions into Ti^{3+} and the number of O sites is three times that of Ti sites.^[49] The Ti oxidation states were determined by fitting the fine structures of Ti-L edge with the linear combination of Ti^{3+} and Ti^{4+} spectra.^[50] As shown in Figure 6e, the fraction of Ti^{3+} was found to be ≈ 0.08 and ≈ 0.3 from the least-squares fittings (blue and brown lines), which corresponds to oxygen deficiency x of ≈ 0.04 and ≈ 0.15 in $Nb:SrTiO_{3-x}$, for the pristine sample and the XPPC sample, respectively. Furthermore, we carried out geometric phase analysis of the HAADF images to characterize the strain states of the samples.^[51] Compared with the homogeneous strain states in both the out-of-plane [001] direction (Figure 6f, component \mathcal{E}_{zz}) and the in-plane [010] direction (Figure 6g, component \mathcal{E}_{yy}) for the pristine sample, the XPPC sample exhibits much stronger local strain fluctuations in the NSTO region (Figure 6i,j), which is induced by the higher concentration of

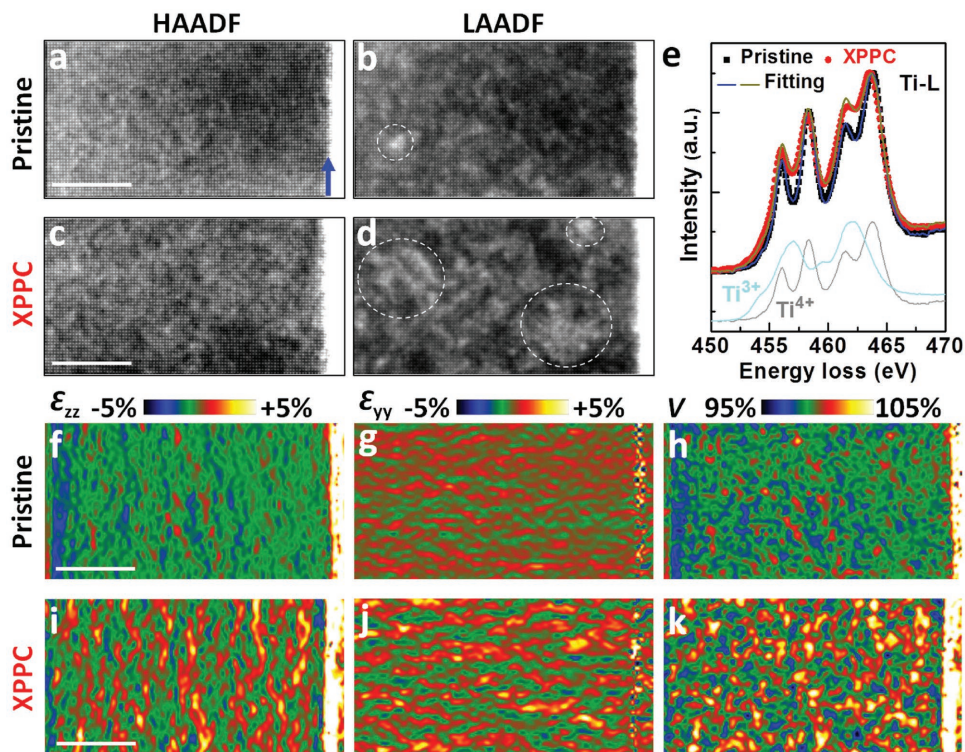


Figure 6. X-ray enhanced aggregation of oxygen vacancies investigated by STEM. HAADF and LAADF images taken on the NSTO side of the pristine sample a,b) and the XPPC sample after X-ray exposure c,d). Blue arrow indicates the interface between NSTO and SBFO. Dashed lines in (b) and (d) mark a few typical oxygen-vacancy-rich regions. e) Electron energy loss spectra (EELS) of Ti-L edge. Oxygen vacancy concentration δ in Nb:SrTiO_{3- δ} was determined by fitting the experimental data using the reference spectra of Ti⁴⁺ and Ti³⁺ taken from NSTO and Ti₂O₃ powders, respectively. Strain component ϵ_{zz} (f,i), ϵ_{yy} (g,j), and the unit cell volume (h,k) obtained from the geometric phase analysis for the pristine sample (f,g,h) and the XPPC sample (i,j,k). Scale bars, 10 nm.

oxygen vacancies. In line with the stronger strain fluctuation, the XPPC sample also showed much more distortions of the unit cell (Figure 6k) compared with the pristine sample (Figure 6h).

3. Discussion

Different from the current-in-plane structures in previous reports, the colossal XPPC effect observed in the NSTO/SBFO heterostructures hinges on the nonvolatile reduction of the interfacial barriers induced by X-ray illumination. Concurrently, a higher concentration of oxygen vacancies with strong local lattice strain was observed near the NSTO/SBFO interface after the X-ray illumination. Based on these observations, we propose a microscopic model to explain the colossal XPPC effect in the NSTO/SBFO heterostructures (Figure 7). This model is based on switchable deep donor point defects (DX centers) which can assume both insulating and conducting behavior, depending on the extent of lattice distortion induced by external excitations such as X-ray radiation.^[10,12,13,15,19,20] In the energy diagram, SBFO is an n-type semiconductor,^[52] and two Schottky barriers ϕ_b of ≈ 0.6 – 0.7 eV are formed at the interfaces between SBFO and Pt electrodes for the pristine state (Figure 7a). Because of the upward ferroelectric polarization of SBFO, NSTO is deeply depleted at the interface with the energy bands bending up. X-ray illumination increases the concentration of oxygen vacancies and efficiently ionizes them from neutral V_O^0 to

charged V_O^{2+} , whose energy levels lie in the conduction band (Figure 7b). As the result, photoexcited electrons are released into the conduction band, reducing the depletion of NSTO. With the aid of the depolarization field, some of these excited electrons diffuse into SBFO and are trapped there, which lifts up the Fermi level of SBFO and reduces the two interface barrier heights to ≈ 0.3 eV, resulting in a conductivity enhancement of 10^6 times. Importantly, the V_O^{2+} state is metastable because of a configuration relaxation occurring during the ionization process, which produces an energy barrier E_a between V_O^{2+} and V_O^0 (Figure S12, Supporting Information). For the system to return to the pristine state, the metastable V_O^{2+} must surmount E_a to go back to the ground state V_O^0 , which results in the slow relaxation of XPPC. Alternatively, E_a could be overcome with the help of thermal excitation, which explains the efficient restoration of the pristine state by thermal annealing (Figure 3c,d).

To shed light on the nature of E_a in the scenario above, we carried out density functional theory (DFT) calculations. As shown in Figure 7c, we considered the influence of an oxygen vacancy at the interfacial TiO₂ layer of BiFeO₃/SrTiO₃ heterostructure and investigated the effect of configuration relaxation accompanied by the ionization of oxygen vacancies. Our calculations reveal that the ground states of V_O^0 and V_O^{2+} correspond to different configurations. Figure 7d shows the calculated oxygen vacancy formation energy (ΔH) as function of configuration (relaxation) coordinates of heterostructure. It can be seen that the minima of ΔH of V_O^0 and V_O^{2+} have different

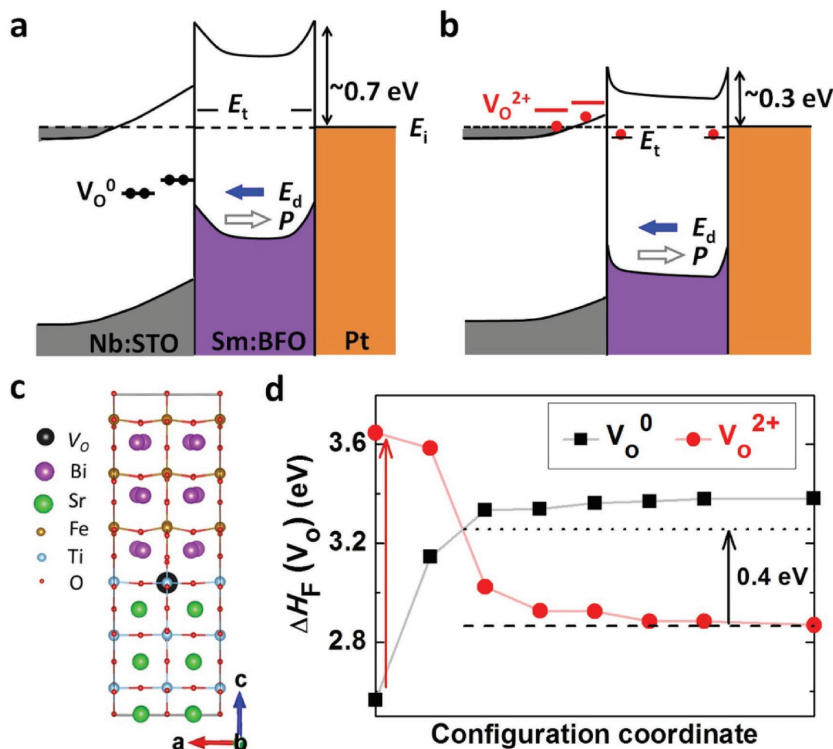


Figure 7. Proposed mechanism for the colossal XPPC effect observed in NSTO/SBFO/Pt heterostructures. Schematic band alignment diagrams for a) the pristine state and b) the XPPC state. V_O^0 and V_O^{2+} represent the neutral and ionized oxygen vacancy, respectively. P denotes the ferroelectric polarization of SBFO, and E_d is the depolarization field. V_O^0 is ionized into V_O^{2+} upon illumination with electrons being excited into the conducting band, which results in the reducing of the NSTO depletion layer width and leads to a large junction conductivity enhancement. The X-ray illumination increases concentration of ionized oxygen vacancies. c) Schematic of the BiFeO₃/SrTiO₃ heterostructure used in the DFT calculations. d) Calculated energy profile of oxygen vacancies as function of configuration coordinates. The configuration coordinates include both electronic and structural degrees of freedom, with major contribution from the former. V_O^0 is the ground state in the absence of illumination. Upon illumination, V_O^0 is ionized into V_O^{2+} (red arrow). Subsequently, V_O^{2+} undergoes a relaxation to low-energy configurations (dashed line). V_O^{2+} is metastable and must be activated across an energy barrier ≈ 0.4 eV (black arrow) to return to V_O^0 , through which the system decays back to the pristine state.

configuration coordinates. In our calculation, the energy difference of these configurations is ≈ 1.1 eV, which might be much smaller than the actual energy if defect complexes and clusters are involved. In fact, it was reported before that X-ray illumination might distort the crystal lattice and facilitate the ionization of oxygen vacancies into the metastable configurations.¹⁵ After V_O^{2+} undergoes relaxation to low-energy configurations, it must be activated across an energy barrier and simultaneously capture two electrons in order to return to the V_O^0 state.^[20] The calculated barrier between these two stable configurations is 0.4 eV (the black arrow in Figure 7d), which is largely consistent with the high energy barrier (≈ 0.6 – 0.8 eV) deduced from the relaxation measurement.

4. Conclusion

In summary, a colossal XPPC effect with a magnitude of 10^6 was observed at room temperature in semiconductor/ferroelectric

thin-film heterostructures with a current-perpendicular-to-plane geometry. This colossal PPC effect originates from the X-ray-induced formation and ionization of oxygen vacancies and the associated reduction of the Schottky barrier heights between the electrodes and the ferroelectric layer. The energy barrier between the stable and metastable lattice configurations causes the PPC in such artificial perpendicular heterostructure. This operating mechanism fundamentally differs from the photon-induced enhancement of carrier density/mobility reported previously for the current-in-plane semiconductor bulks and heterostructures. The discovery of this colossal XPPC effect in such current-perpendicular-to-plane semiconductor/ferroelectric heterostructures provides a new route for the exploration of high-performance X-ray sensing and imaging applications.

5. Experimental Section

Thin Film Growth and Device Fabrication: $\text{Sm}_{0.1}\text{Bi}_{0.9}\text{FeO}_3$ films with different thicknesses were deposited on (001) NSTO substrates via PLD (KrF excimer laser with a wavelength of 248 nm). The films were grown at a temperature of 600 °C, oxygen pressure of 10 mTorr, laser energy density of 1 J cm^{-2} , and repetition rate of 3 Hz. Then, the semitransparent top electrodes (Ti 10 nm/Pt 5 nm, Al 10 nm/Pt 5 nm, Au 10 nm/Pt 5 nm, or Pt 15 nm) were prepared by photolithography and sputtering.^[24] The effective device area was $5 \times 5 \mu\text{m}^2$.

TEM and EELS: Cross-sectional TEM specimens were prepared by Helios Dual Beam system (FEI Co, Netherlands) with about 30 nm thickness of NSTO/SBFO interface area. HR-STEM analyses in combination with EELS was carried out by FEI Titan 60-300 TEM equipped with high-brightness field emission gun (X-feg), Cs-probe corrector, and a Gatan Imaging Filter (Quantum 966). The microscope was operated at 200 kV accelerating voltage. HR-STEM images were collected with a 17 mrad convergence semi-angle of the probe, ≈ 0.14 nm probe size and 100 pA probe current. The inner collection angle of the STEM detector was 55 mrad for HAADF and 22 mrad for LAADF imaging. To improve STEM imaging quality and reduce the effects of sample drift and scanning noise the method of drift corrected frame integration was implemented. For each image a series of 30 frames (2 s per frame) was recorded, and then the off-line postalignment and integration applied to generate a single image with a high signal/noise ratio and minimized distortions. In this way a generalized Geometrical Phase Analysis software package developed by Gutakovskii et al.^[51] can be directly applied to determine 2D strain matrix. HR-STEM imaging was combined with EELS to obtain STEM-EELS spectrum images with a probe size of 0.14 nm and a beam current of 500 pA. The energy dispersion of 0.1 eV and an EELS collection angle of 75 mrad were used.

Electrical Characterizations: PFM and CAFM measurements were performed using a commercial atomic force microscope (Asylum Research MFP-3D) with Pt-coated Si cantilever tips (OSCM-PT). In typical PFM measurements, a 600 mV ac voltage at a contact resonance

frequency of ≈ 280 kHz was applied on the tip. In CAFM measurement, a dc bias voltage of 0.5 V was applied on the sample.

Photoelectric Characterizations: Devices were uniformly illuminated from the top. Wavelengths of 655 to 470 nm (maximum intensity $\approx 0.19\text{--}0.75$ W cm $^{-2}$) were provided by LEDs (Metrohm, Autolab). The 365 nm wavelength (maximum intensity ≈ 7.3 W cm $^{-2}$) was produced by a handheld UV lamp (Agitron, SUVF). The broad-spectrum X-ray beam was generated by a copper tube (Bruker, D8 Advance) with an accelerating voltage of 40 kV and a low dose rate of ≈ 140 $\mu\text{Gy s}^{-1}$. For comparison, typical dose rates are $\approx 1.4\text{--}2800$ $\mu\text{Gy s}^{-1}$ for diagnostic medical applications.^[53] The X-ray beam was centered on the sample and an illumination time of ≈ 10 s was applied to trigger the PPC effect. Electrical measurements (293–473 K) were performed on a micro-manipulated probe station (Microtech, MPS150) equipped with a multi-SourceMeter (Keithley, 2635A). Capacitance was measured using an LCR meter (Agilent E4980A) with a frequency range from 20 Hz to 20 MHz. A clean indium piece was mechanically pressed onto the corner of the NSTO surface to make ohmic contacts. In all measurements, the positive voltage corresponds to current flowing from the top electrode to the bottom NSTO electrode.

Density-Functional Calculations: A defect model was considered in which an oxygen atom was removed from the interfacial TiO $_2$ layer of 3(SrTiO $_3$) $_3$ (BiFeO $_3$) supercell, as shown in Figure 7c. BiFeO $_3$ was strained to the STO in-plane lattice, while *c/a* and the internal coordinates of the overall supercell were optimized. For the calculations, DFT was used with pseudopotential generated using projector augmented-wave methods^[54,55] and exchange and correlation approximated with local density approximations (LDA). The exchange and correlation beyond LDA was approximated by utilizing spherically symmetric Hubbard U_i ^[56] with $U = 5$ eV for Ti and $U = 3$ eV for Fe 3d orbitals such that the overall heterostructure without defect was insulating. $4 \times 4 \times 4$ k-points mesh were used for Brillouin zone integration and a 340 eV kinetic energy cutoff. The calculations were spin polarized with the G-type antiferromagnetic spin arrangement.

Supporting Information

Supporting Information is available from the Wiley Online Library or from the author.

Acknowledgements

This work was supported by King Abdullah University of Science and Technology (KAUST). The research at University of Nebraska-Lincoln was supported by the National Science Foundation through the Nebraska Materials Research Science and Engineering Center (Grant No. DMR-1420645).

Conflict of Interest

The authors declare no conflict of interest.

Keywords

ferroelectrics, oxygen vacancies, persistent photoconductivity, Schottky junctions, X-ray

Received: July 31, 2017
Revised: October 22, 2017
Published online:

- [1] A. Rose, *Concepts in Photoconductivity and Allied Problems*, Wiley, London **1963**.
- [2] D. Casa, V. Kiryukhin, A. Saleh, B. Keimer, J. P. Hill, Y. Tomioka, Y. Tokura, *Europhys. Lett.* **1999**, *47*, 90.
- [3] B. Keimer, D. Casa, V. Kiryukhin, O. A. Saleh, J. P. Hill, Y. Tomioka, Y. Tokura, *Mater. Sci. Eng.* **1999**, *B63*, 30.
- [4] K. H. Schoenbach, V. K. Lakdawala, R. Germer, S. T. Ko, *J. Appl. Phys.* **1988**, *63*, 2460.
- [5] D. C. Stoudt, M. A. Richardson, F. E. Peterkin, *IEEE Trans Plasma Sci.* **1997**, *25*, 131.
- [6] M. C. Tarun, F. A. Selim, M. D. McCluskey, *Phys. Rev. Lett.* **2013**, *111*, 187403.
- [7] P. J. Snyder, R. Kirste, R. Collazo, A. Ivanisevic, *Small* **2017**, *13*, 1700481.
- [8] H. X. Jiang, J. Y. Lin, *Phys. Rev. Lett.* **1990**, *64*, 2547.
- [9] A. Bhatnagar, Y. H. Kim, D. Hesse, M. Alexe, *Nano Lett.* **2014**, *14*, 5224.
- [10] R. L. Field III, Y. Jin, H. Cheng, T. Dannecker, R. M. Jock, Y. Q. Wang, C. Kurdak, R. S. Goldman, *Phys. Rev. B* **2013**, *87*, 155303.
- [11] P. Feng, I. Mönch, S. Harazim, G. S. Huang, Y. F. Mei, O. G. Schmidt, *Nano Lett.* **2009**, *9*, 3453.
- [12] Y. Soh, G. Aeppli, F. M. Zimmermann, E. D. Isaacs, A. I. Frenkel, *J. Appl. Phys.* **2001**, *90*, 6172.
- [13] S. H. Dietze, M. J. Marsh, S. M. Wang, J. G. Ramirez, Z. H. Cai, J. R. Mohanty, I. K. Schuller, O. G. Shpyrko, *Phys. Rev. B* **2014**, *90*, 165109.
- [14] A. Tebano, E. Fabbri, D. Pergolesi, G. Balestrino, E. Traversa, *ACS Nano* **2012**, *6*, 1278.
- [15] V. Kiryukhin, D. Casa, J. P. Hill, B. Keimer, A. Vigliante, Y. Tomioka, Y. Tokura, *Nature* **1997**, *386*, 813.
- [16] A. Rastogi, J. J. Pulikkotil, R. C. Budhani, *Phys. Rev. B* **2014**, *89*, 125127.
- [17] J. Z. Li, J. Y. Lin, H. X. Jiang, M. A. Khan, Q. Chen, *J. Appl. Phys.* **1997**, *82*, 1227.
- [18] H. J. Queisser, *Phys. Rev. Lett.* **1985**, *54*, 234.
- [19] D. J. Chadi, K. J. Chang, *Phys. Rev. B* **1989**, *39*, 10063.
- [20] S. Lany, A. Zunger, *Phys. Rev. B* **2005**, *72*, 035215.
- [21] A. Q. Jiang, C. Wang, K. J. Jin, X. B. Liu, J. F. Scott, C. S. Hwang, T. A. Tang, H. B. Lu, G. Z. Yang, *Adv. Mater.* **2011**, *23*, 1277.
- [22] Z. Wen, C. Li, D. Wu, A. Li, N. B. Ming, *Nat. Mater.* **2013**, *12*, 617.
- [23] E. Y. Tsybal, A. Gruverman, *Nat. Mater.* **2013**, *12*, 602.
- [24] W. J. Hu, Z. H. Wang, W. L. Yu, T. Wu, *Nat. Commun.* **2016**, *7*, 10808.
- [25] B. C. Jeon, D. Lee, M. H. Lee, S. M. Yang, S. C. Chae, T. K. Song, S. D. Bu, J. S. Chung, J. G. Yoon, T. W. Noh, *Adv. Mater.* **2013**, *25*, 5643.
- [26] R. Kohlrausch, *Ann. Phys. Chem.* **1854**, *91*, 179.
- [27] J. C. Phillips, *Phys. Rev. B* **1995**, *52*, R8637.
- [28] J. C. Phillips, *Rep. Prog. Phys.* **1996**, *59*, 1133.
- [29] H. X. Jiang, J. Y. Lin, *Phys. Rev. B* **1989**, *40*, 10025.
- [30] A. Dissanayake, M. Elahi, H. X. Jiang, J. Y. Lin, *Phys. Rev. B* **1992**, *45*, 13996.
- [31] I. Bahar, B. Erman, G. Fytas, W. Steffen, *Macromolecules* **1994**, *27*, 5200.
- [32] Y. Yamada, T. Nakamura, S. Yasui, H. Funakubo, Y. Kanemitsu, *Phys. Rev. B* **2014**, *89*, 035133.
- [33] A. Bera, H. Y. Peng, J. Lourembam, Y. D. Shen, X. W. Sun, T. Wu, *Adv. Funct. Mater.* **2013**, *23*, 4977.
- [34] W. Ramadan, S. B. Ogale, S. Dhar, L. F. Fu, S. R. Shinde, D. C. Kundaliya, M. S. R. Rao, N. D. Browning, T. Venkatesan, *Phys. Rev. B* **2005**, *72*, 205333.
- [35] J. Frenkel, *Phys. Rev.* **1938**, *54*, 647.
- [36] H. Yang, M. Jain, N. A. Suvorova, H. Zhou, H. M. Luo, D. M. Feldmann, P. C. Dowben, R. F. Depaula, S. R. Foltyn, Q. X. Jia, *Appl. Phys. Lett.* **2007**, *91*, 072911.
- [37] I. Stolichnov, A. Tagantsev, *J. Appl. Phys.* **1998**, *84*, 3216.

- [38] A. Rose, *Phys. Rev.* **1955**, *97*, 1538.
- [39] L. Pintilie, I. Vrejoiu, D. Hesse, G. Lerhun, M. Alexe, *Phys. Rev. B* **2007**, *75*, 104103.
- [40] S. J. Clark, J. Robertson, *Appl. Phys. Lett.* **2007**, *90*, 132903.
- [41] L. L. Hench, J. K. West, *Principles of Electronic Ceramics*, Wiley, New York **1990**.
- [42] G. Singh-Bhalla, C. Bell, J. Ravichandran, W. Siemons, Y. Hikita, S. Salahuddin, A. F. Hebard, H. Y. Hwang, R. Ramesh, *Nat. Phys.* **2010**, *7*, 80.
- [43] Y. Li, R. Yao, H. H. Wang, X. M. Wu, J. Z. Wu, X. H. Wu, W. Qin, *ACS Appl. Mater. Interfaces* **2017**, *9*, 11711.
- [44] S. X. Wu, X. Luo, S. Turner, H. Y. Peng, W. N. Lin, J. F. Ding, A. David, B. Wang, G. V. Tendeloo, J. L. Wang, T. Wu, *Phys. Rev. X* **2013**, *3*, 041027.
- [45] K. A. Brown, S. He, D. J. Eichelsdoerfer, M. C. Huang, I. Levy, H. Lee, S. Ryu, P. Irvin, J. Mendez-Arroyo, C. B. Eom, C. A. Mirkin, J. Levy, *Nat. Commun.* **2016**, *7*, 10681.
- [46] N. Poccia, M. Fratini, A. Ricci, G. Campi, L. Barba, A. Vittorini-Orgeas, G. Bianconi, G. Aeppli, A. Bianconi, *Nat. Mater.* **2011**, *10*, 733.
- [47] A. Howie, *J. Microsc.* **1979**, *17*, 11.
- [48] E. J. Kirkland, R. F. Loane, J. Silcox, *Ultramicroscopy* **1987**, *23*, 77.
- [49] D. A. Muller, N. Nakagawa, A. Ohtomo, J. L. Grazul, H. Y. Hwang, *Nature* **2004**, *430*, 657.
- [50] A. Ohtomo, D. A. Muller, J. L. Grazul, H. Y. Hwang, *Nature* **2002**, *419*, 378.
- [51] A. K. Gutakovskii, A. L. Chuvilin, S. A. Song, *Bull. Russ. Acad. Sci.: Phys.* **2007**, *71*, 1426.
- [52] H. T. Yi, T. Choi, S. G. Choi, Y. S. Oh, S. W. Cheong, *Adv. Mater.* **2011**, *23*, 3403.
- [53] I. Clairand, J. M. Bordy, E. Carinou, J. Dures, J. Debroas, M. Denoziere, L. Donadille, M. Ginjaume, C. Itie, C. Koukorava, S. Krim, A. L. Lebacqz, P. Martin, L. Struelens, M. Sans-Merce, F. Vanhavere, *Radiat. Meas.* **2011**, *46*, 1252.
- [54] P. E. Blöchl, *Phys. Rev. B* **1994**, *50*, 17953.
- [55] G. Kresse, J. Joubert, *Phys. Rev. B* **1999**, *59*, 1758.
- [56] S. L. Dudarev, G. A. Botton, S. Y. Savrasov, C. J. Humphreys, A. P. Sutton, *Phys. Rev. B* **1998**, *57*, 1505.